Electronic Supplementary Information

Combined intercalation and space-charge mechanism enabled high-capacity, ultrafast and long-lifespan sodium-ion storage for chalcogenides anodes

Feilong Pan,[a] Zhao Li,[ab] Shiyu Yao,*[a] Jingyi Liu,[a] Zhixuan Wei,*[a] Xiao Chen,[c] Yu Xie*[ab] and Fei Du*[a]

[a]Key Laboratory of Physics and Technology for Advanced Batteries (Ministry of Education), State Key Laboratory of Superhard Materials, College of Physics, Jilin University, Changchun, 130012, China.

[b]Key Laboratory of Material Simulation Methods and Software of Ministry of Education, College of Physics, Jilin University, Changchun, 130012, China.

[c]Beijing Key Laboratory of Green Chemical Reaction Engineering and Technology, Department of Chemical Engineering, Tsinghua University, Beijing, 100084, China.

Experimental methods

Materials synthesis:

$3R\text{-}NbS_2$ was synthesized via a simple solid reaction method from Nb (Aladdin, 99.5%), and S (Sigma Aldrich, 99.8%, 5 wt% excess). Specifically, high purity powder of Nb (0.01mol) and S (0.0205mol) were mixed thoroughly and sealed in quartz tube under vacuum. Then the sample was heated to 750 °C with a rate of 5°C min^{-1} and kept at that temperature for 24 h, followed by cooling to room temperature with a rate of 1.5 °C min^{-1}.

Characterization method:

X-ray diffraction (XRD) patterns were conducted by a Rigaku D/max-2550 diffractometer with Cu-Kα radiation, and Rietveld refinement using FullProf software was carried out for the crystal structure analysis. The morphology information and elemental analysis of the samples were obtained by field emission scanning electron microscopy and energy dispersive spectroscopy (Regulus 8100). The microstructure of the samples was further evaluated using a TEM instrument (JEM-2100F) equipped with a probe corrector operating at 200 kV. The STEM imaging was conducted in a Cs-corrected scanning transmission electron microscope (FEI Titan Cubed Themis G2 300) operated at 300 kV. This microscope is equipped with a DCOR+ spherical aberration corrector for the electron probe, which was aligned with proper aberration coefficients using a standard gold sample. The convergence semi-angle is 24 mrad. The beam current is about 30 pA (measured by a pixel array detector). Fourier transform infrared (FTIR) spectra was conducted on a VERTEX 80v Fourier Transform Infrared Spectrometer. Raman spectra was obtained on a inVia Raman spectrometer. Ultraviolet-visible (UV-vis) absorption spectra was conducted on a PerkinElmer Lambda 1050+ spectrophotometer. X-ray photoemission spectra (XPS) was carried out using a Thermo Scientific K-Alpha spectrometer. X-ray absorption fine structure (XAFS) spectroscopy was investigated using a RapidXAFS 1M (Anhui Absorption Spectroscopy Analysis Instrument Co., Ltd.) by transmission mode at 20 kV and 40

mA, and the Si (553) spherically bent crystal analyzer with a radius of curvature of 500 mm was used for Cu. The thermogravimetric (TG) analysis measurements were performed on a Rigaku TG-DTA 8122 simultaneous thermal analyzer with a heating rate of 10 ºC/min from room temperature to 600 ºC in N_2 atmosphere. The time-of-flight second ion mass spectroscopy (TOF-SIMS) was employed using a TESCAN C-TOF SIMS spectrometer. Before measurement, the electrodes were washed with DME in the glove box to get rid of the electrolyte.

Electrochemical measurement:

The electrochemical performances were evaluated by assembling the CR2032 coin type half-cells in the argon filled glovebox. For fabrication of electrodes, active materials, super P and sodium alginate (SA) binder were mixed in a weight ratio of 7:2:1 with loading mass of 1.0-1.5 mg cm^{-2}. The above mixture was dissolved in de-ionized water. Then the slurry was casted on Cu foil current collector and dried at 60 ° C for 12 h under vacuum. Higher mass loading electrodes (5.9-6.8 mg cm^{-2}) were also manufactured using the above method. The compacted density of the NbS_2 electrodes are 0.47 g cm^{-3}. The sodium metal was functioned as the counter electrode, and the glass fiber filters (Whatman GF/C) was employed as the separator. 1 m $NaPF_6$ dissolved in DME was principally employed as the electrolyte for testing, while 1 m $NaPF_6$ dissolved in EC/DEC was also used for comparison. For fabrication of the conductive-additive-free electrode, active materials and SA binder were mixed in a weight ratio of 19:1. For universality study, Na–TiS_2, Na–TaS_2, and Na–$NbSe_2$ half-cells were prepared using commercial TiS_2 (Aladdin, 99.5%), TaS_2 (Nanjing Muke, 99.95%), and $NbSe_2$ (Nanjing Muke, 99.95%) particles and the same procedures. The compacted density of the TiS_2, TaS_2 and $NbSe_2$ electrodes are 0.34 g cm^{-3}, 0.64 g cm^{-3} and 0.49 g cm^{-3}, respectively. The galvanostatic tests were carried out by using Land-2001A (Wuhan, China) automatic battery tester and VSP multichannel potentiostatic-galvanostatic system (Bio-Logic SAS, France). EIS, GITT and CV were performed on a VSP multichannel potentiostatic-galvanostatic system (Bio-Logic SAS, France). For the Na-ion full cells, the cathode was assembled by mixing 70 wt % $Na_3V_2(PO4)_3$

(NVP), 20 wt % Super p, and 10 wt % poly(vinylidene fuoride) (PVDF) as binder coated on aluminum foil. The compacted density of the NVP electrodes are 0.31 g cm^{-3}. The mass ratio of anode/cathode was controlled to be about 1:1.5. Meanwhile, the anode was electrochemically activated 10 cycles at 0.1 A g^{-1} for pre-sodiation before it was assembled in full cells.

DFT calculations:

All DFT calculations were performed using the Vienna Ab initio Simulation Package (VASP)[S1] employing the projector augmented-wave (PAW) method.[S2] The Perdew-Burke-Ernzerhof (PBE) generalized gradient approximation (GGA)[S3] functional was adopted for all calculations. A plane wave energy cutoff of 600 eV and Monkhorst-Pack k-point grids with a resolution of $2\pi \times 0.03$ Å^{-1} were employed for structural relaxations and energy calculations. The energies and forces for structural relaxations were converged to 10^{-6} eV per cell and 0.01 eV Å^{-1}, respectively.

Structure enumeration and phase diagram:

The experimentally determined $Cu_{0.43}NbS_2$ structure has partial occupation on Cu sites. We made a 2×2×1 supercell and set the occupancy of Cu to 0.417 to get integer number of Cu atoms (resulting in the formula $Cu_5Nb_{12}S_{24}$) and best match the experimental data within the limits of computational capabilities. All symmetrically distinct structures of $Cu_5Nb_{12}S_{24}$ were found by the enumlib[S4] wrapper in Python Materials Genomics (pymatgen)[S5] and fully optimized. The lowest-energy configuration was chosen for subsequent analysis. The phase stability of $Cu_5Nb_{12}S_{24}$ was estimated by calculating its energy above the convex hull within the Nb-S-Cu phase diagram, which was constructed by pymatgen, with energies for compounds in the phase diagram obtained from the Materials Project database.[S6]

To clarify the impact of DME molecule intercalation, we constructed supercells with formulas $Nb_{48}S_{96}$ and $Cu_{20}Nb_{48}S_{96}$, and introduced a single DME molecule. Density of States (DOS), band structures and electron localization functions (ELF)[S7] were calculated to assess the influence of DME molecule and Cu intercalation on the

electronic properties of NbS_2. Additionally, a $Nb_{96}S_{192}$ supercell with a DME molecule intercalated was created to evaluate the effect of DME intercalation on the interlayer spacing of NbS_2.

NEB calculation:

Climbing image nudged elastic method was used to determine the migration barriers of Cu moving from surface into the interior of NbS_2. A vacuum thickness of 15 Å was adopted to avoid inter-action between two adjacent periodic images. The initial guess for the minimum energy path was constructed with six linearly interpolated intermediate images. A Γ-centered 1×1×1 k-point grid was used , and the forces on every atom were finally converged to less than 0.05 eV/Å.

Energy changes in embedding and adsorption:

The reaction of Cu intercalated into TMDs (MX_2) was defined by the following equation:

$$MX_2 \square\square + nCu = Cu_n MX_2$$
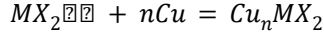
The change of Gibbs free energy ΔG was calculated as

$$\Delta G = \frac{[G_{Cu_n MX_2} - G_{MX_2} - n \times G_{Cu}]}{n}$$

where $G_{Cu_n MX_2}$ and G_{MX_2} are the energy of TMDs after and before Cu intercalation. G_{Cu} is the energy required by taking one Cu atom from bulk Cu. n is the number of intercalated Cu atom with up to 5. The ΔG is negative, indicating that Cu atom prefers to intercalate into TMDs rather than forming bulk Cu.

The adsorption energy of Na absorbed by Cu cluster was calculated by the following formula

$$E_{ads} = \frac{G_{total} - G_{cluster} - n \times G_{Na}}{n}$$

where G_{total} is the energy after system adsorption, $G_{cluster}$ is the Gibbs free energy of Cu cluster, G_{Na} is the energy required by taking one Na atom from bulk Na. n is the number of absorbed Na atom, with up to 17 for decahedron Cu cluster and 30 for icosahedron Cu cluster. A negative E_{ads} represent that Cu cluster can absorb Na atoms effectively.

# Spontaneous co-intercalation behavior of Cu and ether into NbS$_2$
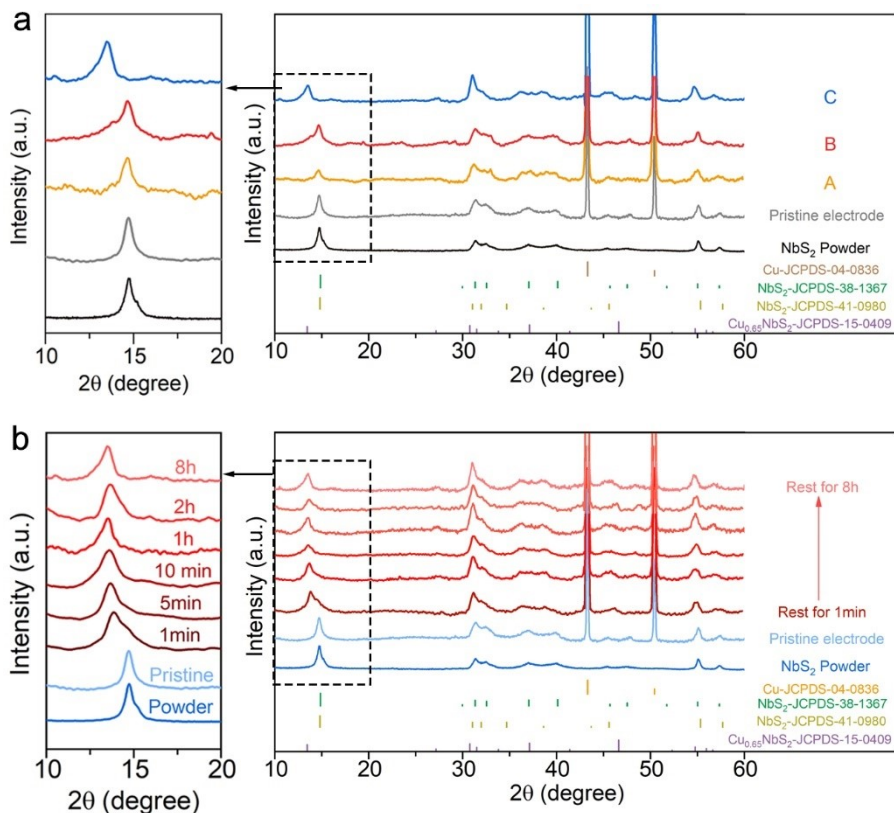
Fig. S1 (a) XRD patterns of the NbS$_2$ electrodes after different treatment. A : NbS$_2$ electrode was soaked in ether-based electrolyte for 8 hours; B : NbS$_2$ electrode after being assembled in a half cell with NaPF$_6$ in EC/DEC for 8 hours; C : NbS$_2$ electrode after being assembled in a half cell with NaPF$_6$ in DME for 8 hours. (b) XRD patterns of the NbS$_2$ electrodes after being assembled in a half cell with NaPF$_6$ in DME for different rest time.
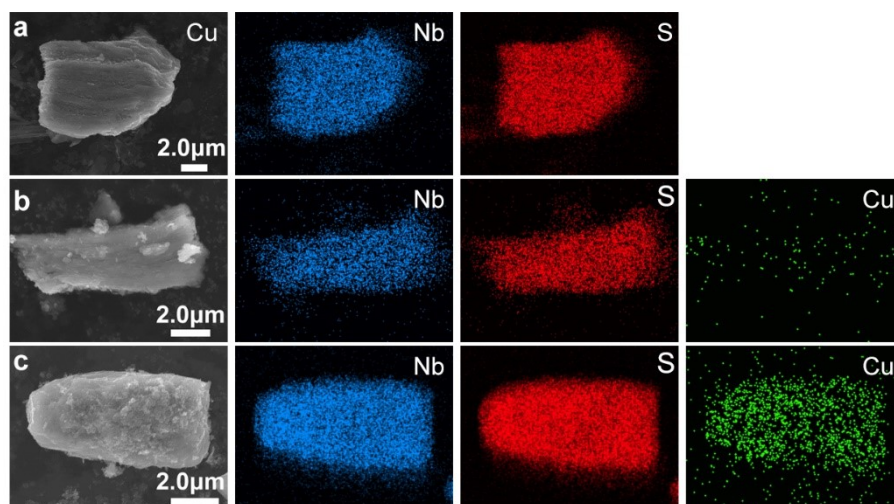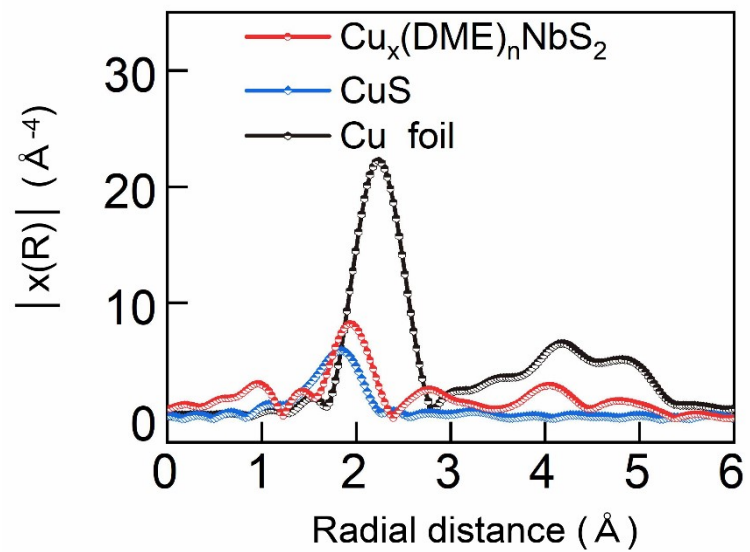
Fig. S2 SEM images and element maps of powder. (a) NbS$_2$ powder. (b) NbS$_2$ electrode after being assembled in a half cell with NaPF$_6$ in EC/DEC. (c) NbS$_2$ electrode after being assembled in a half cell with NaPF$_6$ in DME.
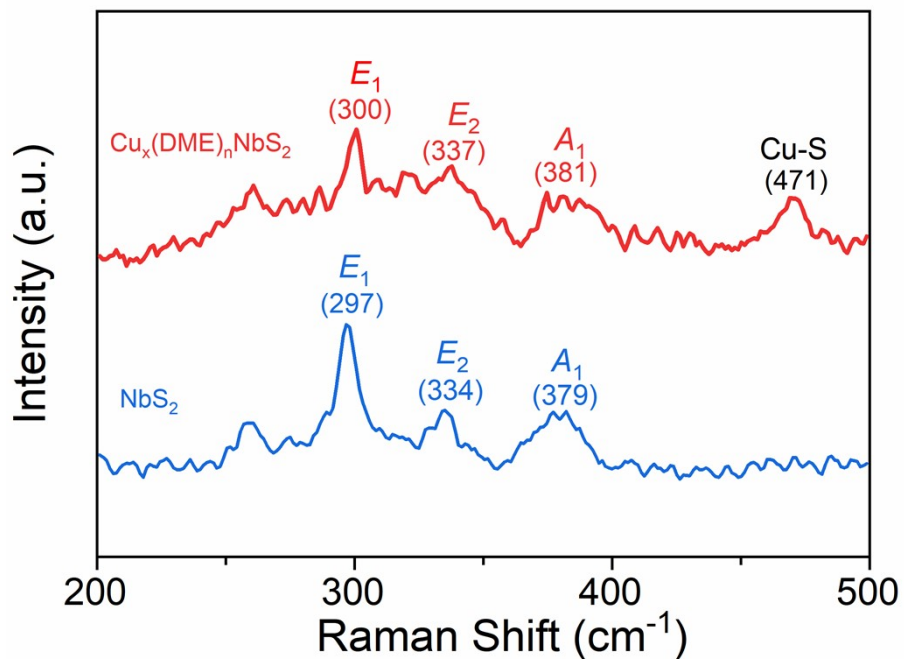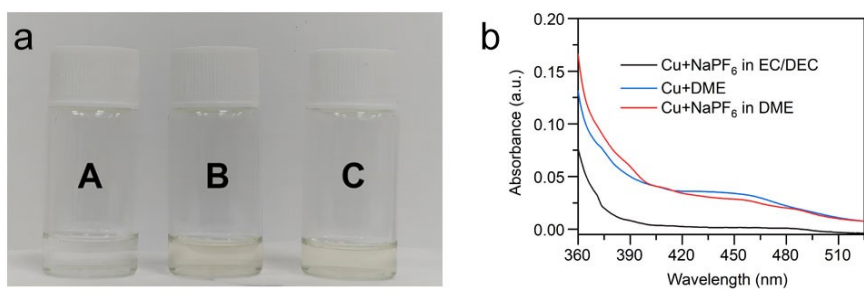
**Fig. S3** Raman spectrum of NbS_2 and $Cu_x(DME)_nNbS_2$.
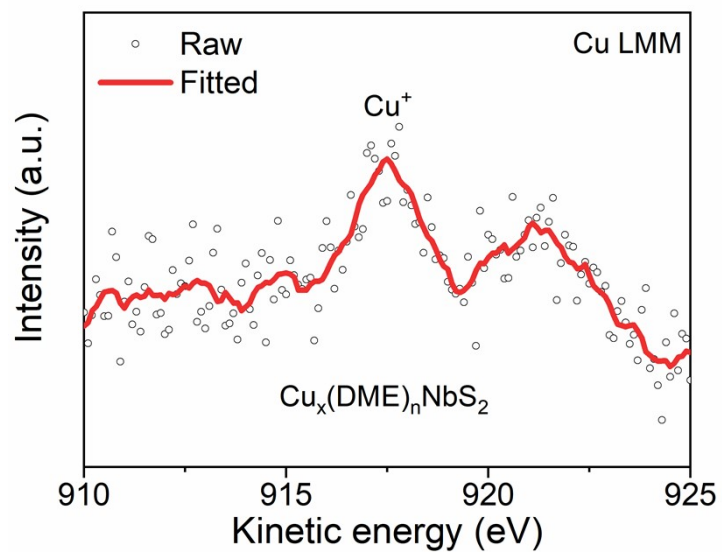
Fig. S4 Cu LMM Auger spectra of $Cu_x(DME)_nNbS_2$.

Fig. S5 EXAFS at the Cu K-edge for $Cu_x(DME)_nNbS_2$ and corresponding reference samples.

Fig. S6 Optical image and UV-vis absorption spectroscopy. (a) Optical image of Cu foil immersing in the different solutions for 48h, A : NaPF$_6$ in EC/DEC; B : DME; C : NaPF$_6$ in DME. (b) UV-vis absorption spectroscopy of Cu foil immersing in the different solutions for 48h.
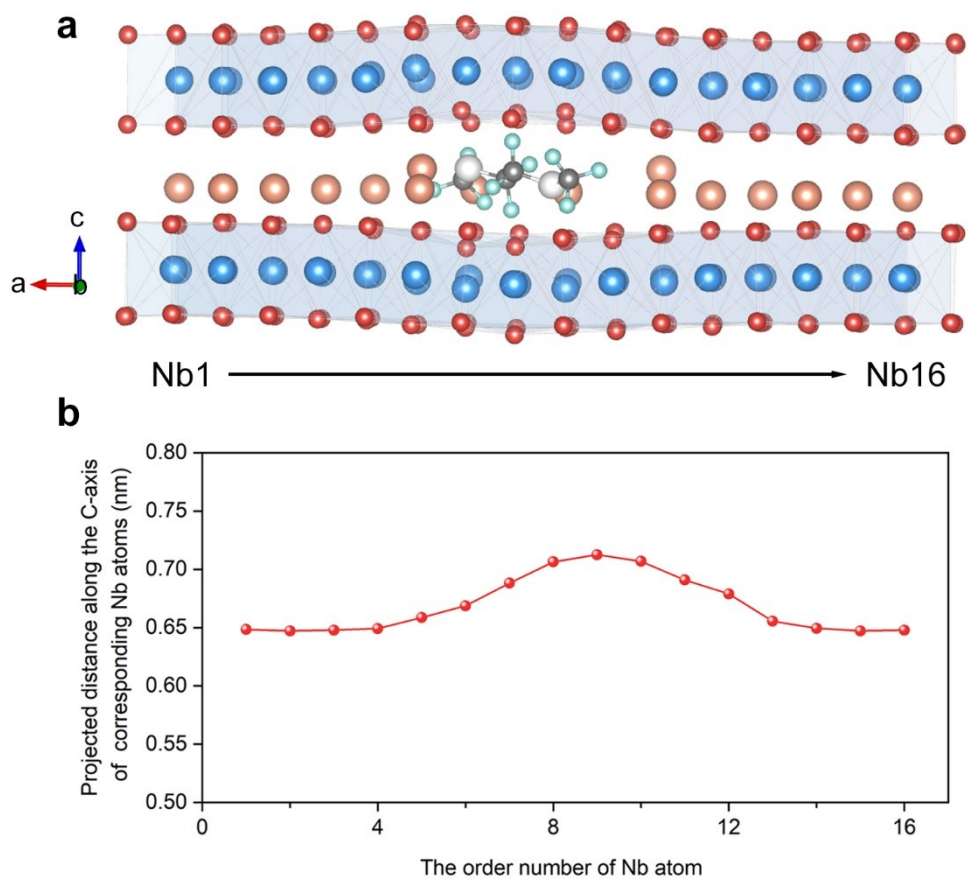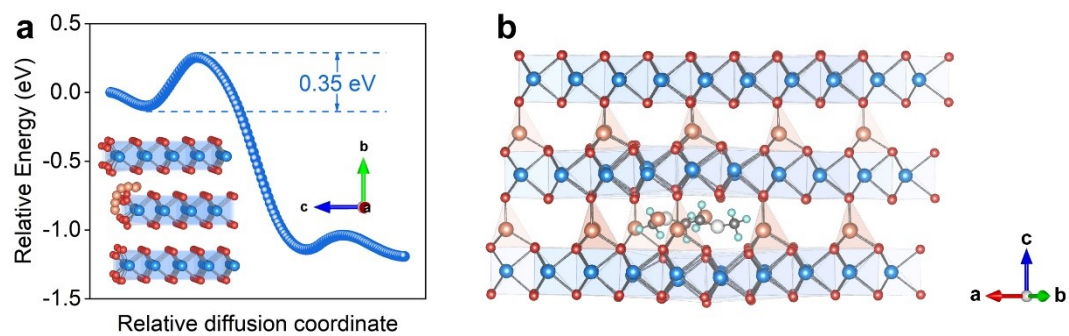
Fig. S7 (a) The $Cu_{20}(DME)Nb_{48}S_{96}$ structure used in calculation. (b) The vertical distance of corresponding Nb atoms.
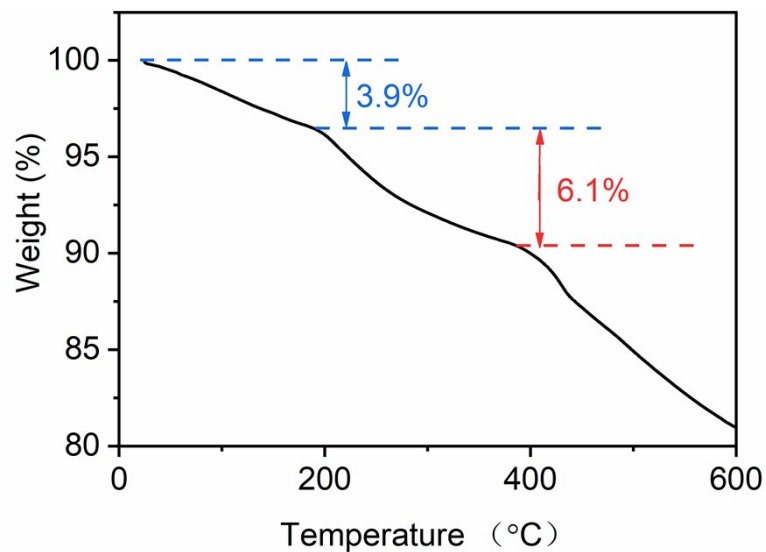
Fig. S8 TG data of the $Cu_x(DME)_nNbS_2$.

$Cu_x(DME)_nNbS_2$ exhibits a two-step weight loss, which can be ascribed to the removal of adhered water (before 200 °C) and DME (between 200 and 400 °C) within the structure, respectively. Note that further weight loss above 400 °C might be related to the thermal decomposition of the transition metal sulfide.[S8]

Fig. S9 (a) The calculated barrier for a Cu atom migrating from the surface layer into the interior of NbS_2. The inset figure shows the calculated migrating path of Cu. (b) The $Cu_{20}(DME)Nb_{48}S_{96}$ structure used in calculation.
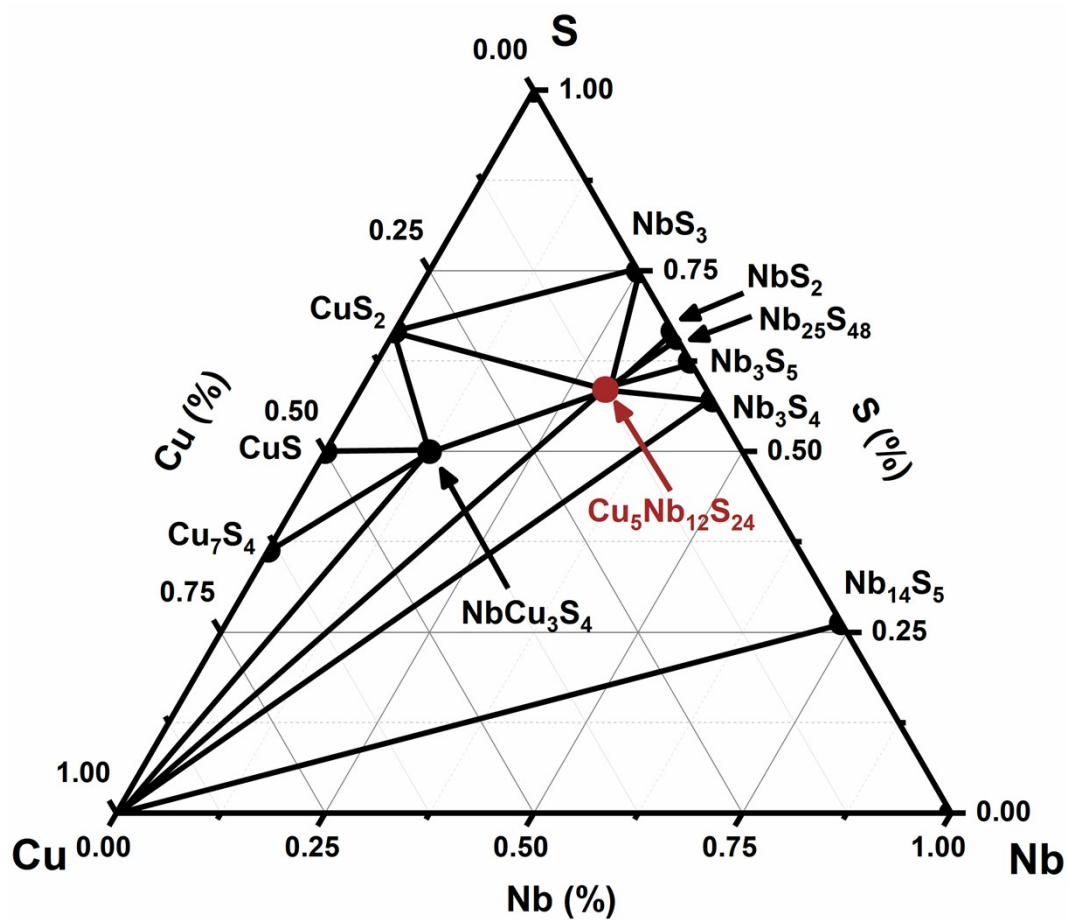
Fig. S10 The Cu-Nb-S ternary phase diagram constructed by pymatgen. All compounds

shown in the figure are thermodynamically stable.

Sodium storage properties
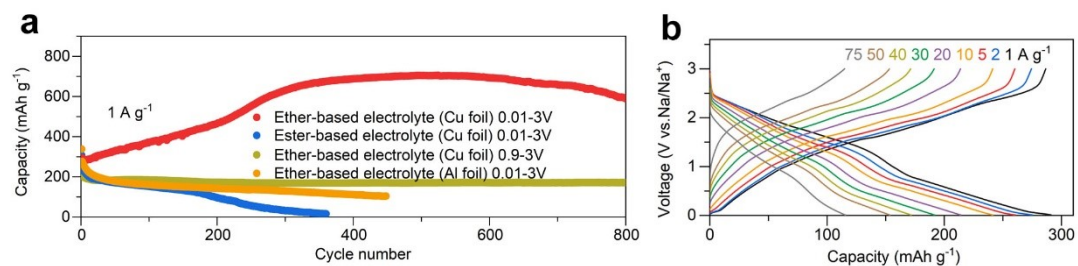
Fig. S11 Electrochemical performances of sodium half cells. (a) The cycling performance of different NbS_2 electrodes. (b) The galvanostatic charge and discharge profiles of the $Cu_{0.43}DME_{0.12}NbS_2$ electrode at the various current densities.
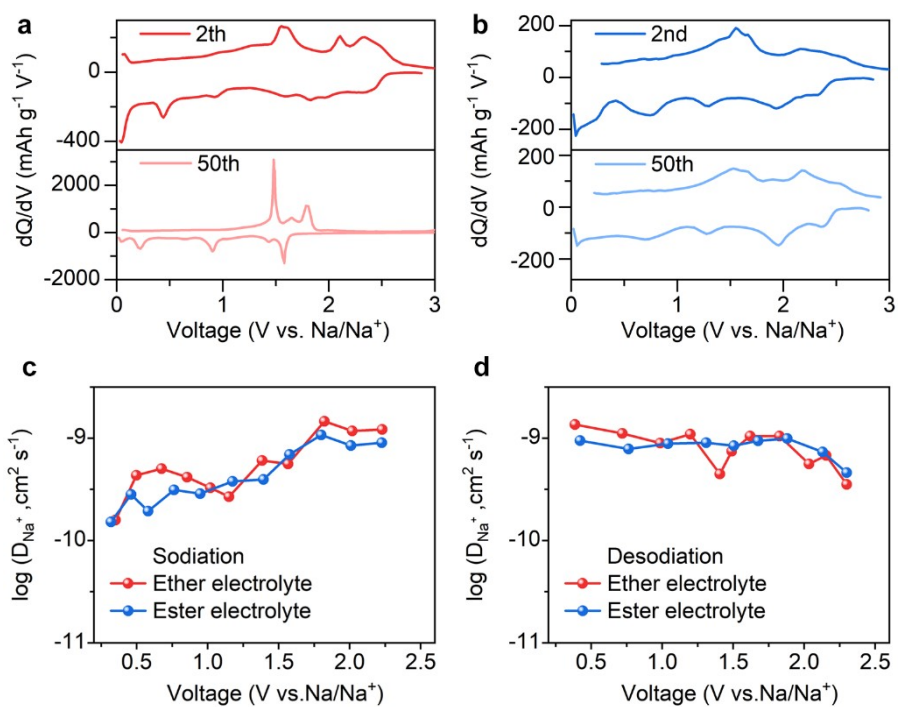
Fig. S12 The dQ/dV curves of the NbS_2 electrodes at 0.1 A g^{-1} using (a) $NaPF_6$ in DME and (b) $NaPF_6$ in EC/DEC as the electrolytes. Na^+ diffusion coefficients of the NbS_2 electrodes using different electrolytes calculated from the GITT results. (c) sodiation. (d) desodiation.
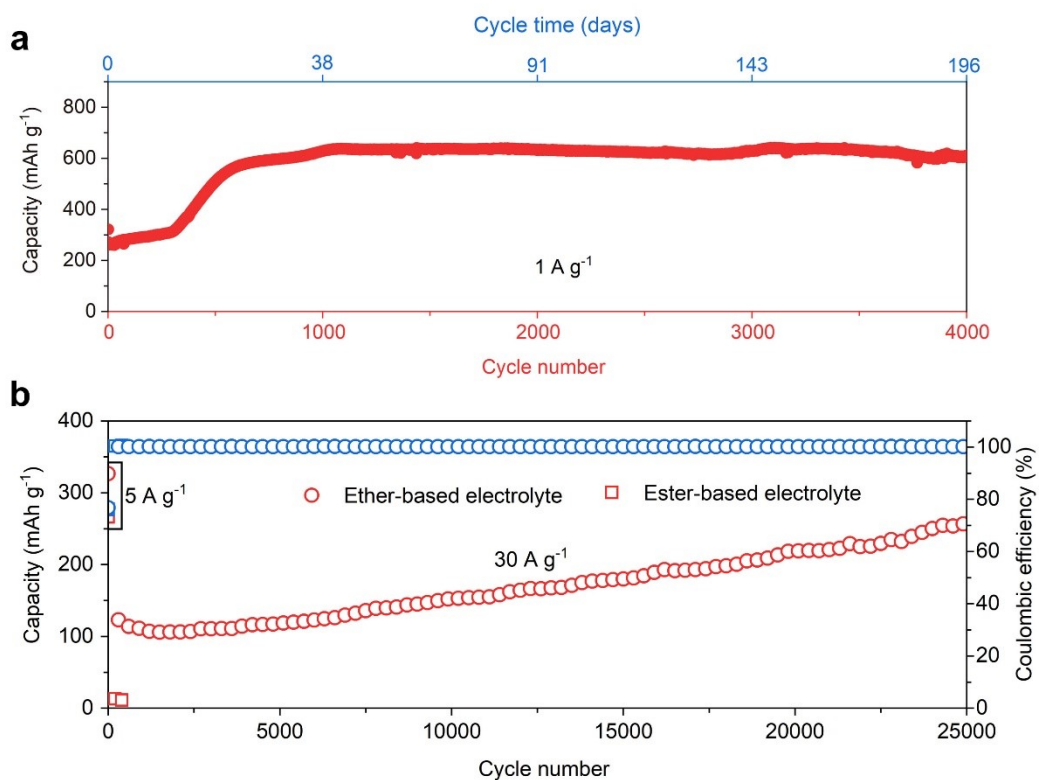
Fig. S13 (a) Long cycle performance at 1 A g^{-1} in the voltage of 0.3-3.0 V. The top axis shows the corresponding cycle time. The voltage range is set to 0.3-3.0 V to prevent the decomposition of ether electrolytes at low voltage. (b) Long cycle performance at 30 A g^{-1} in the voltage of 0.01-3.0 V.
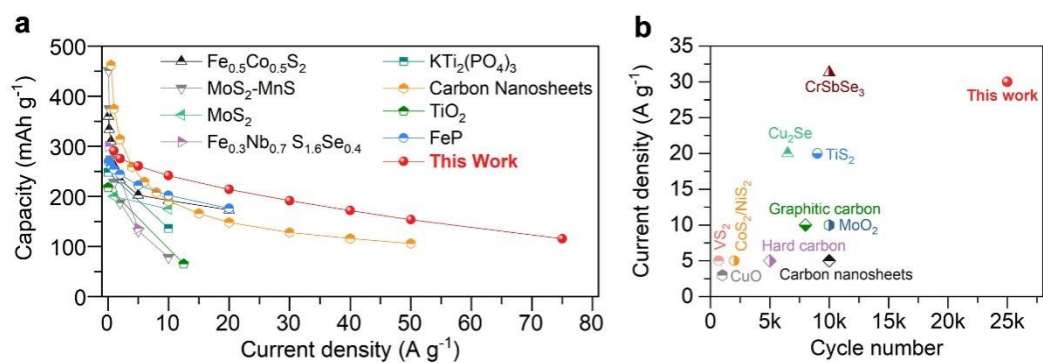
Fig. S14 (a) Comparison of the rate performance between the $Cu_{0.43}DME_{0.12}NbS_2$ electrode and previously reported different anodes.[S9-S16] (b) Comparison of the cyclic stability at high current densities between the $Cu_{0.43}DME_{0.12}NbS_2$ electrode and previously reported different anodes.[S16-S25]
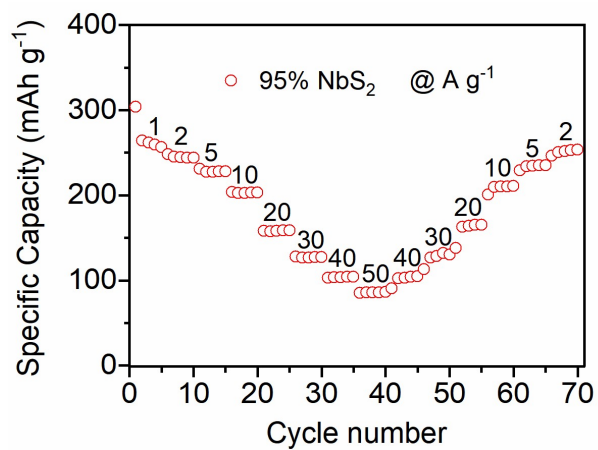
Fig. S15 Rate performance of the conductive-additive-free electrode. For fabrication of the conductive-additive-free electrode, active materials and SA binder were mixed in a weight ratio of 19:1.
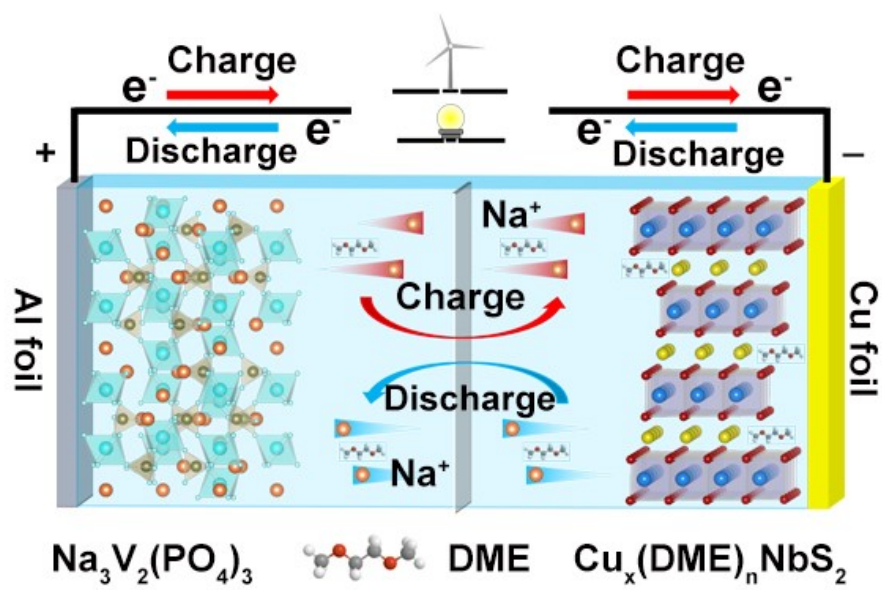
Fig. S16 Scheme of the NVP// $Cu_{0.43}DME_{0.12}NbS_2$ full cell.
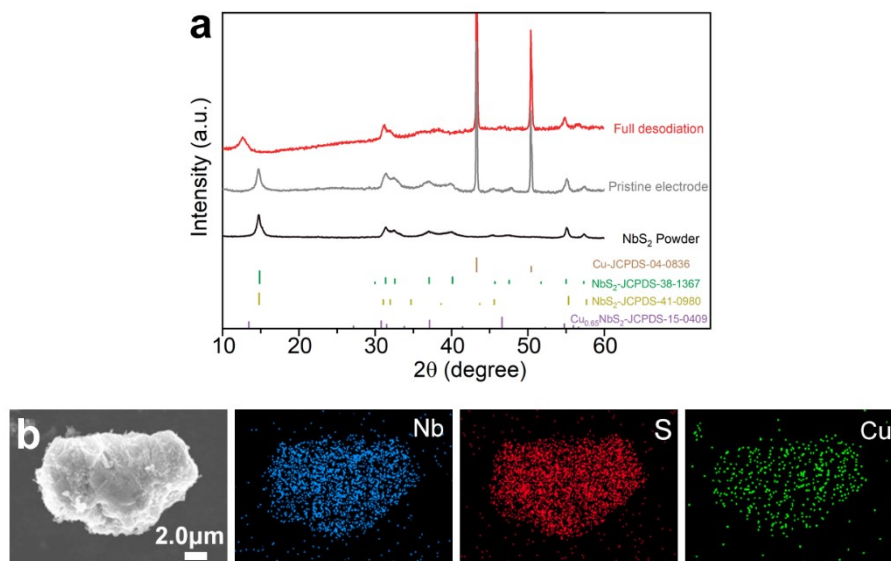
Fig. S17 (a) XRD patterns and (b) Element maps of the NbS$_2$ electrode in the full cell configuration after 40 cycles. The full cell uses Na$_3$V$_2$(PO$_4$)$_3$ as the cathode and pure NbS$_2$ as the anode without pre-intercalated Cu ions.

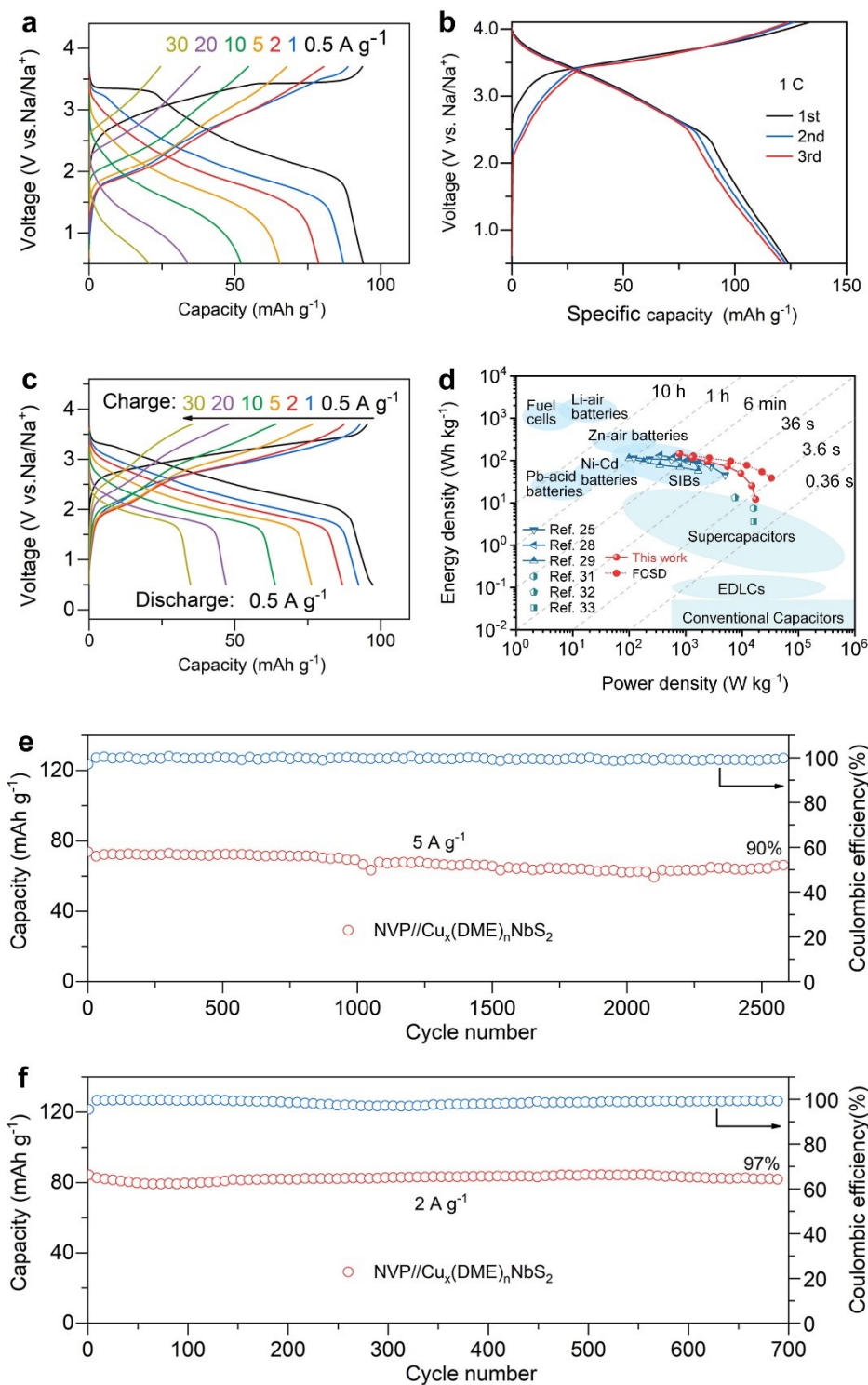**Fig. S18** Electrochemical performances of the full cell. (a) The galvanostatic charge and discharge profiles of NVP// $Cu_{0.43}DME_{0.12}NbS_2$ at the various current densities. (b) The galvanostatic charge and discharge profiles of $NaNi_{0.33}Fe_{0.33}Mn_{0.33}O_2$// $Cu_{0.43}DME_{0.12}NbS_2$. The mass loading ratio of the cathode and anode is 10.2 : 4.1 mg

cm^{-2}. (c) The galvanostatic charge and discharge profiles of NVP// $Cu_{0.43}DME_{0.12}NbS_2$ at the various charging current densities and a discharging current density of 0.5 A g^{-1}. (d) Ragone plots of the NVP// $Cu_{0.43}DME_{0.12}NbS_2$ full cell compared with the current energy-storage systems.[S26-S34] (e-f) The cycling performance of NVP// $Cu_{0.43}DME_{0.12}NbS_2$.
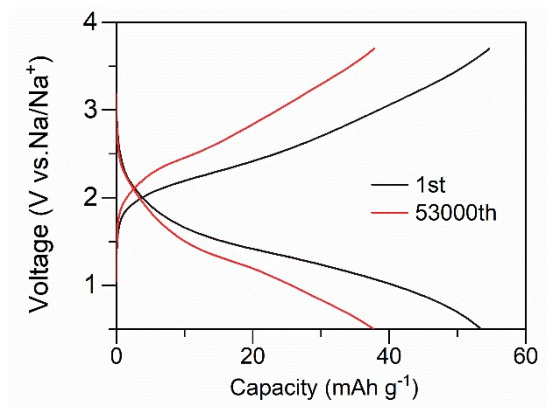
Fig. S19 GCD curves of NVP// $Cu_{0.43}DME_{0.12}NbS_2$ at 10 A g^{-1}.
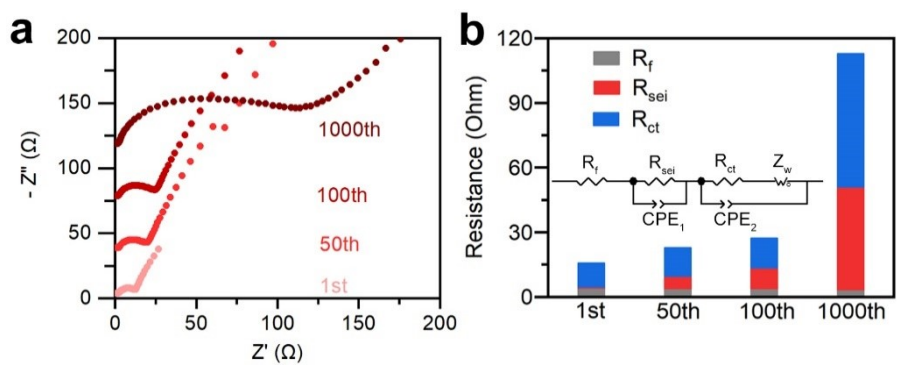
Fig. S20 (a) Nyquist plots of the NVP cathode with the DME-based electrolytes at different cycles. (b) Resistance comparison at different cycles. Inset shows the equivalent circuit.
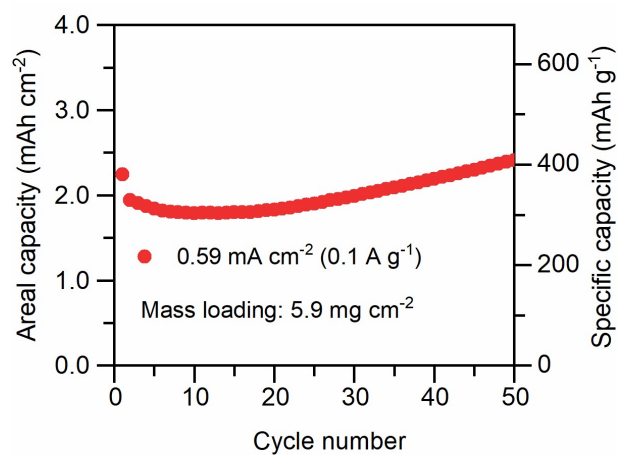
Fig. S21 Electrochemical performances of high mass loading electrodes. The cycle performance of the half cell. The mass loading of the NbS_2 electrode is 5.9 mg cm^{-2}, corresponding to the thickness of 125.5 μm.

Sodium intercalation-space charge reaction mechanism
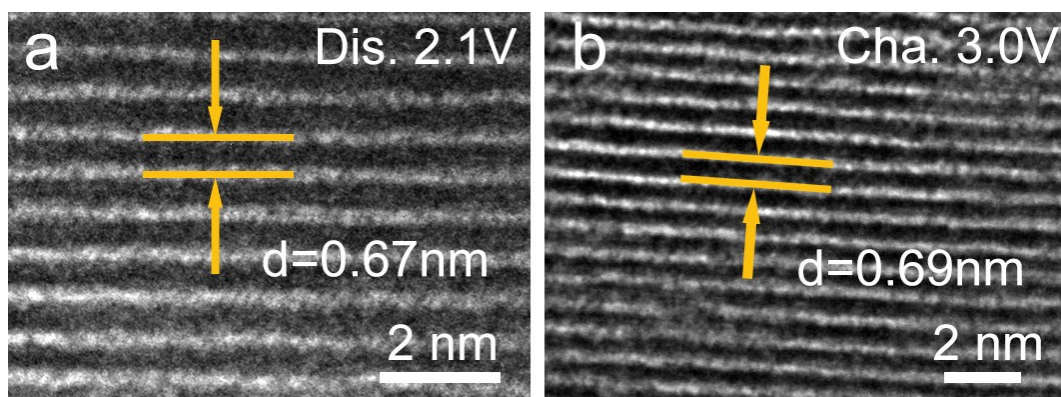
Fig. S22 The HRTEM images of the $Cu_{0.43}DME_{0.12}NbS_2$ electrodes during the first cycle. (a) Being discharged to 2.1 V. (b) Being charged to 3.0 V.
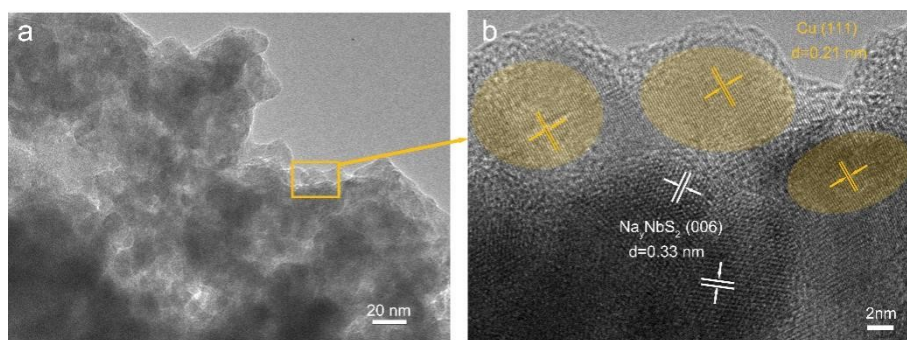
Fig. S23 (a) TEM and (b) HRTEM images of the $Cu_{0.43}DME_{0.12}NbS_2$ electrode after 100 cycles at 0.01V.
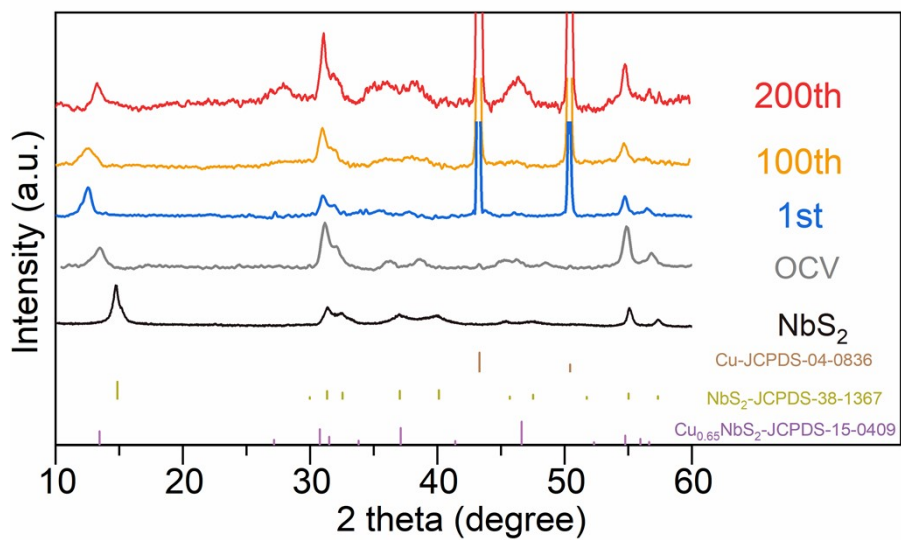
Fig. S24 The NbS$_2$ electrodes after different cycles at 0.01V using NaPF$_6$ in DME as the electrolyte.
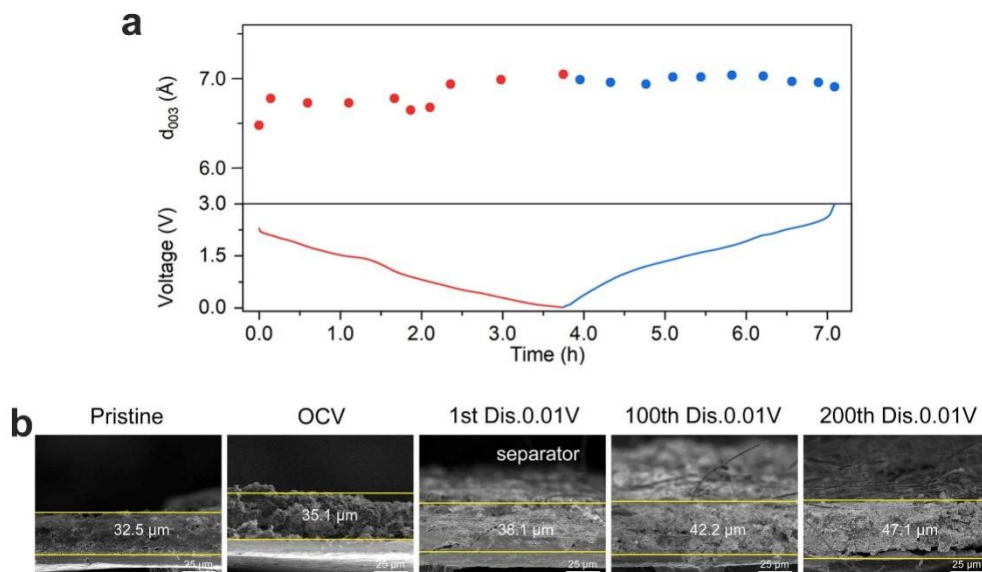
Fig. S25 (a) The layer spacing of the $Cu_{0.43}DME_{0.12}NbS_2$ electrode during the first charge-discharge process. (b) SEM of the electrode in cross-view after different cycles.
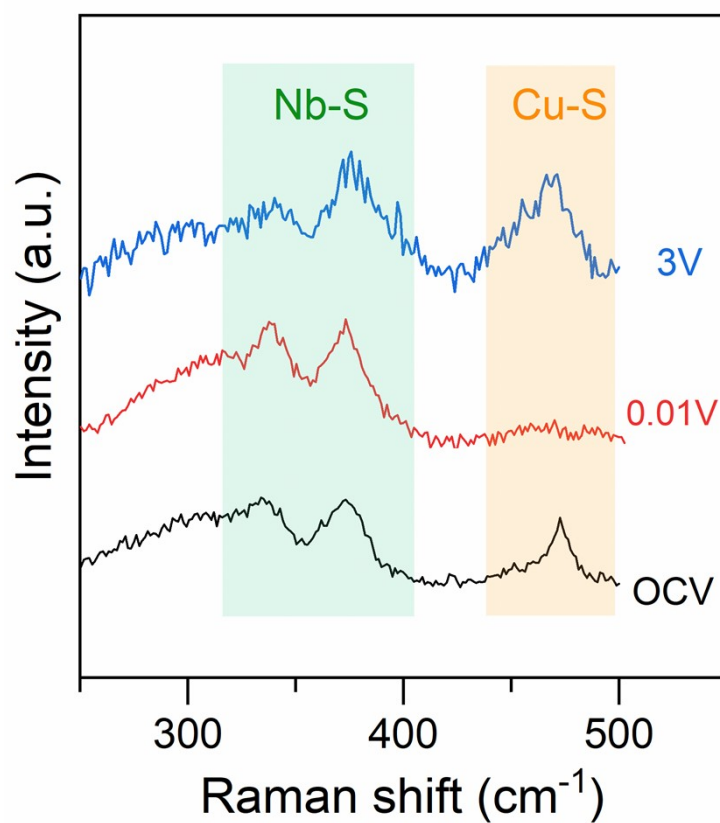
Fig. S26 Ex-situ Raman spectrum of the $Cu_{0.43}DME_{0.12}NbS_2$ electrodes after 100 cycles at different discharge-charge states.

As presented in Fig. 3b and Fig. S25, Raman spectra show a recovery of the Cu-S peak at 3.0 V in the first cycle, and the break and reconstruction of Cu-S bond can still be observed in the 100th cycle, suggestive of an excellent reversibility.
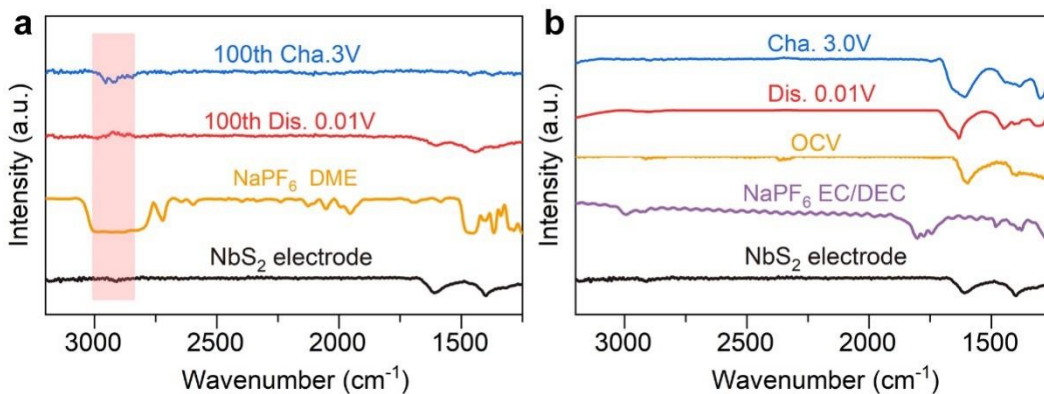
Fig. S27 Ex-situ FTIR spectrum. (a) The NbS$_2$ electrodes after 100 cycles at different discharge-charge states using NaPF$_6$ in DME as the electrolyte. (b) The NbS$_2$ electrodes at different discharge-charge states during the first cycle using NaPF$_6$ in EC/DEC as the electrolyte.

In Fig. 3c and Fig. S26a, the stretching vibration peaks of CH$_2$ in DME appear in the range of 2800 to 3000 cm^{-1} at the OCV state, while disappearing when discharged to 0.01V at the initial and 100th cycle. When charging back to 3.0 V in the first and 100th cycle, the peaks around 2800 to 3000 cm^{-1} recovered, suggesting a highly reversible Cu-ether co-intercalation process that Cu$^+$-DME reoccupies the interlayer space where Na ions take off, which is not observed in NbS$_2$ electrode (Fig. S26b).
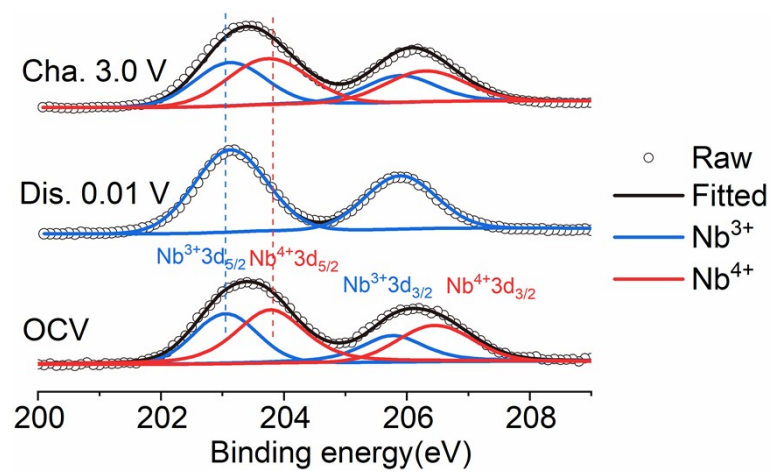
Fig. S28 Ex situ high-resolution XPS spectra of Nb 3d during the first cycle.

| a | b | c | d |
| Pristine powder | Pristine electrode | 100th | 200th |
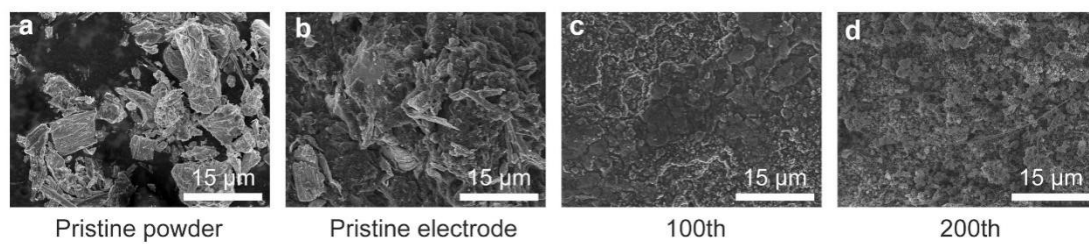
Fig. S29 (a) The SEM images of the synthesized NbS_2. SEM images of the $Cu_{0.43}DME_{0.12}NbS_2$ electrodes after different cycles. (b) Pristine electrode. (c) 100th. (d) 200th.
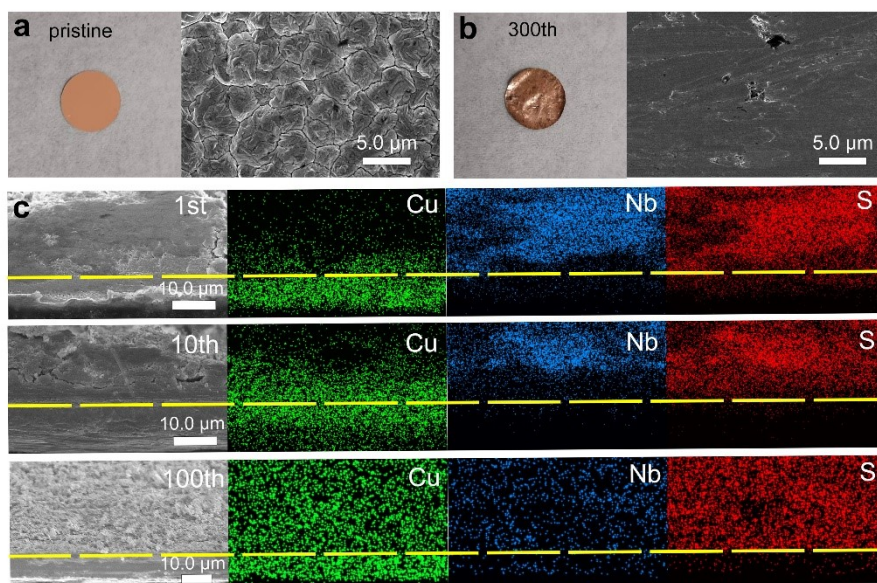
Fig. S30 Optical and SEM images of the Cu foil matt surface (a) before and (b) after cycling.The matt surface of single-light Cu foil is usually used to coat the cathode material. (c) SEM images and element maps of cross-section after different number of cycles.
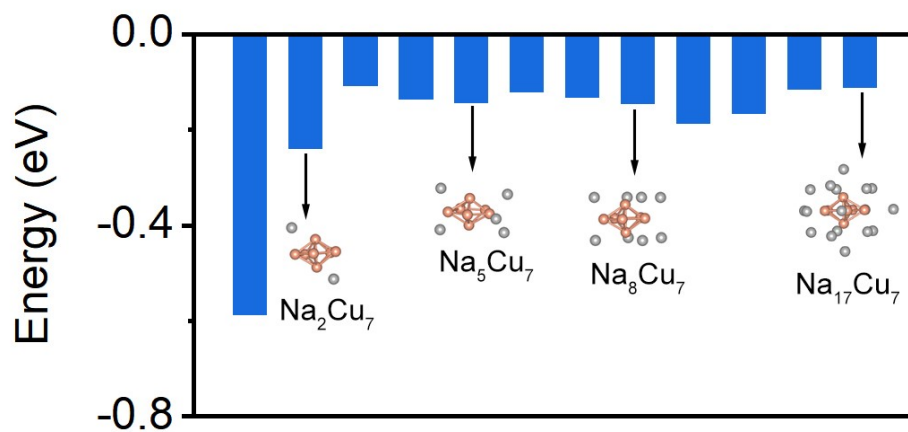
Fig. S31 The calculated absorption energy of Cu_7 cluster for different amounts of Na. The inset shows the structure of Cu_7 clusters adsorbing 2,5,8,17 sodium atoms, respectively.
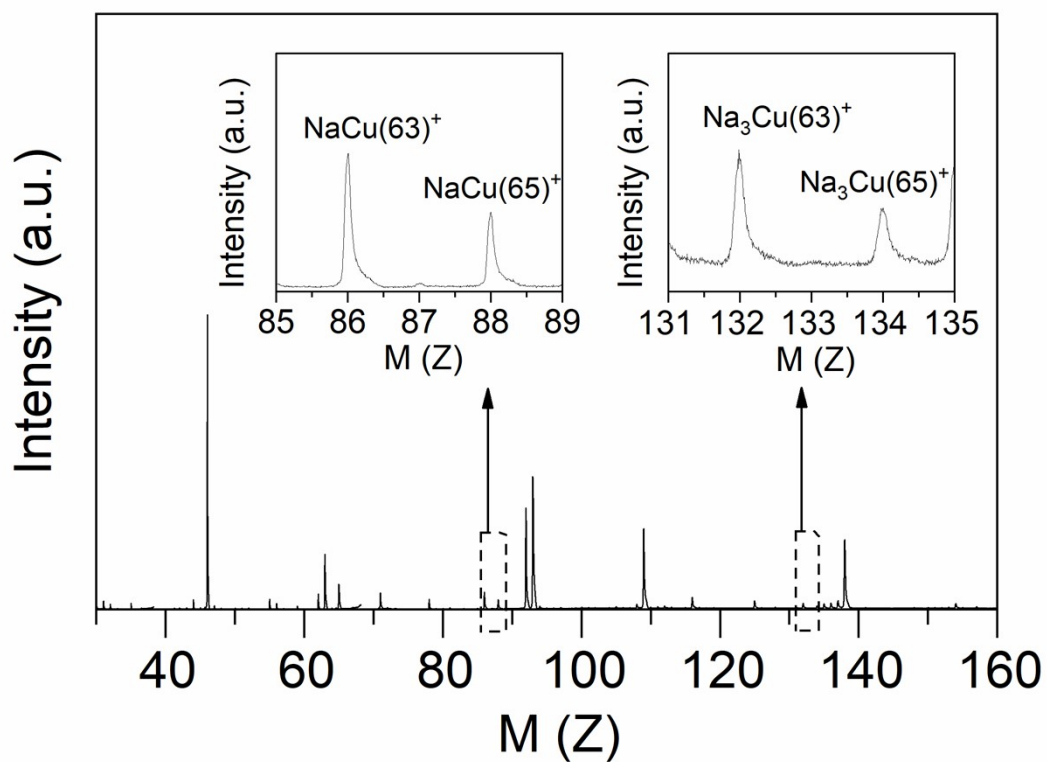
Fig. S32 Mass spectra of the $Cu_{0.43}DME_{0.12}NbS_2$ electrode after 200 cycles at 0.01V.

Mixed ionic-electronic conducting kinetics
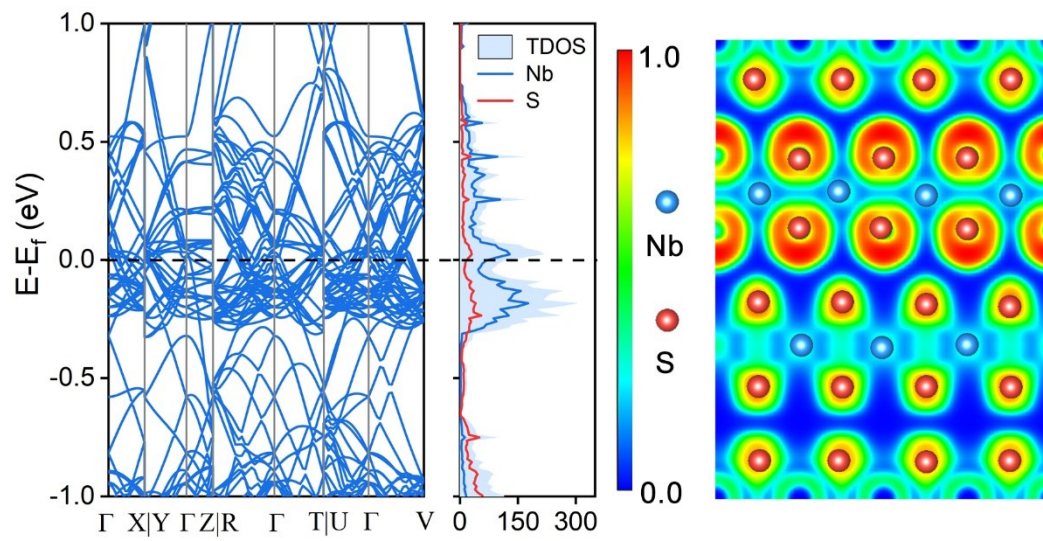
Fig. S33 The band structure, DOS, and ELF maps of $Nb_{48}S_{96}$.
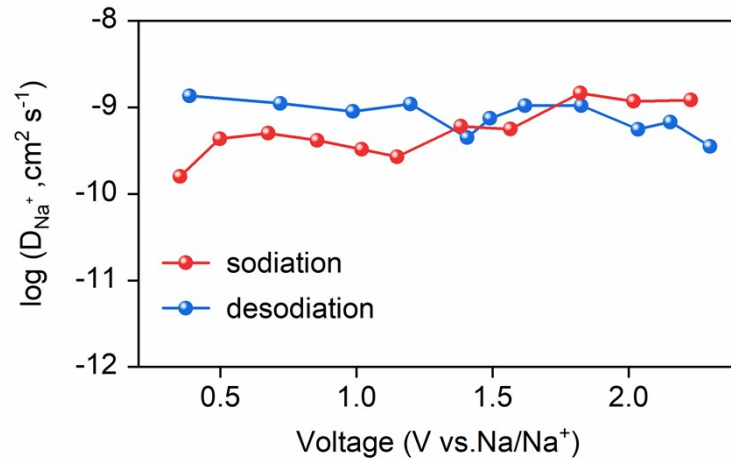
Fig. S34 Na$^+$ diffusion coefficients of the Cu$_{0.43}$DME$_{0.12}$NbS$_2$ electrode calculated from the GITT results.
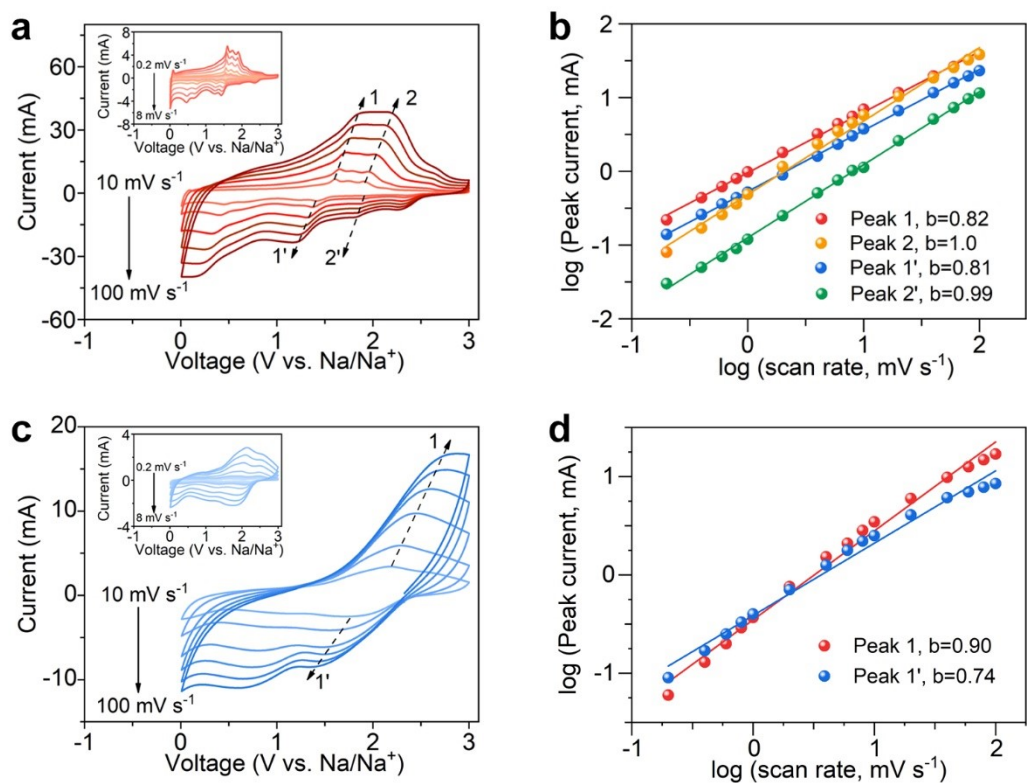
Fig. S35 CV curves acquired at different scan rates from 0.2 to 100 mV s^{-1} and the b-value calculated from plotting the peak current versus scan rate. (a-b) Using NaPF$_6$ in DME as the electrolyte. (c-d) Using NaPF$_6$ in EC/DEC as the electrolyte.

Methodology in other Ternary transition metal dichalcogenide (TMDs)
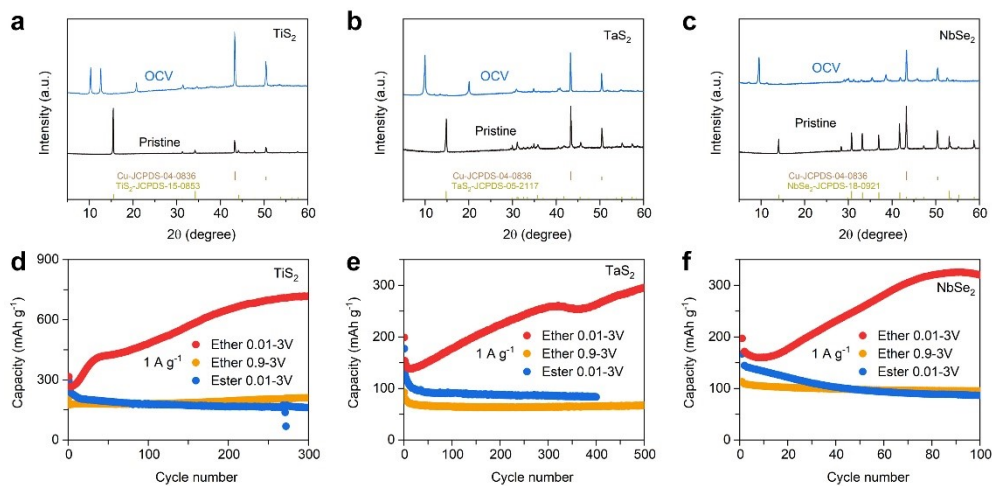
Fig. S36 XRD patterns and cycle performances of the TiS$_2$ electrode, TaS$_2$ electrode and NbSe$_2$ electrode. (a), (d) TiS$_2$. (b), (e) TaS$_2$. (c), (f) NbSe$_2$.

Supplementary Tables

Table S1. Rietveld refinement results of NbS$_2$.

NbS$_2$					
R_{wp}=6.89%, R_p=5.43%					
R3m a = b =3.32995 Å, c =18.01118 Å, α=β=90°, γ=120°					
Atom	Wyckoff.	x	y	z	Occupacy
Nb	3a	0	0	0	1
S1	3a	0	0	0.25096	1
S2	3a	0	0	0.42748	1

Table S2. Rietveld refinement results of $Cu_{0.43}NbS_2$.

		$Cu_{0.43}NbS_2$			
		R_{wp}=2.83%, R_p=2.23%			
R3m	a = b =3.34698 Å,	c =19.49980 Å,	$\alpha=\beta=90°$,	$\gamma=120°$	
Atom	Wyckoff.	x	y	z	Occupacy
Cu	3a	0	0	0.14082	0.431
Nb	3a	0	0	0	1
S1	3a	0	0	0.25	1
S2	3a	0	0	0.41516	1

Table S3. Energy-dispersive X-ray spectroscopy (EDS) analysis of NbS$_2$ and Cu$_{0.43}$NbS$_2$.

| Element | NbS$_2$ | | Cu$_{0.43}$NbS$_2$ | |
	Wt %	At %	Wt %	At %
Nb	58.32	32.56	51.36	30.21
S	41.68	67.44	33.11	56.44
Cu	-	-	15.52	13.35

Table S4. Once discharge time corresponding to different current densities in a half cell.

Time for once discharge (s)	Current density (A g^{-1})	rate (1 C = 0.171 A g^{-1})
1321	1	5.8
599	2	11.7
216	5	29.2
95	10	58.5
40	20	117.0
24	30	175.4
16	40	233.9
12	50	292.4
6	75	438.6

Table S5. Comparison of cycle performance of some advanced sodium anode materials at a current density of 1 A g^{-1}.

Materials	Mass loading (mg cm^{-2})	Cycle number	Cycle time (days)	Ref.
MoS$_{1.5}$Te$_{0.5}$@C	1.2	500	15	S35
GeP$_3$/C	1	2000	117	S36
Sn/FeSn$_2$@C	-	1500	58	S37
FeS@NS-C	1.2	2000	69	S38
graphitic carbon	1.2	10000	107	S23
Bi nanotube	1-1.2	5000	150	S39
C-NTC	1.2	5000	40	S40
This work	1-1.5	4000	196	

The cycle time is estimated using the following formula: $T = \dfrac{2A}{C}N$ where T is Cycle time. A is Average specific capacity. N is Cycle number. C is Current density.

Table S6. EDS analysis of the $Cu_{0.43}DME_{0.12}NbS_2$ electrode powder at different cycle.

Element	OCV (At%)	1st (At%)	100th (At%)
S	56.44	53.58	15.84
Nb	30.21	30.47	7.67
Cu	13.35	15.95	76.50

Supplementary references

S1 G. Kresse and J. Furthmüller, *Phys. Rev. B*, 1996, **54**, 11169.

S2 P. E. Blöchl, *Phys. Rev. B*, 1994, **50,** 17953-17979.

S3 J. P. Perdew, K. Burke and M. Ernzerhof, *Phys. Rev. Lett.*, 1996, **77**, 3865-3868.

S4 G. L. W. Hart and R. W. Forcade, *Phys. Rev. B*, 2008, **77**, 224115.

S5 S. P. Ong, W. D. Richards, A. Jain, G. Hautier, M. Kocher, S. Cholia, D. Gunter, V. L. Chevrier, K. A. Persson and G. Ceder, *Comput. Mater. Sci.*, 2013, **68**, 314-319.

S6 A. Jain, S. P. Ong, G. Hautier, W. Chen, W. D. Richards, S. Dacek, S. Cholia, D. Gunter, D. Skinner, G. Ceder and K. A. Persson, *APL Mater.*, 2013, **1**, 011002.

S7 A. D. Becke and K. E. Edgecombe, *J. Chem. Phys.* 1990, **92**, 5397-5403.

S8 C. Schuffenhauer, G. Wildermuth, J. Felsche and R. Tenne, *Phys. Chem. Chem. Phys.*, 2004, **6**, 3991-4002.

S9 Z. Hu, L. Wang, K. Zhang, J. Wang, F. Cheng, Z. Tao and J. Chen, *Angew. Chem., Int. Ed.*, 2014, **53**, 12794-12798.

S10 K. Zhang, M. Park, L. Zhou, G. H. Lee, J. Shin, Z. Hu, S. L. Chou, J. Chen and Y. M. Kang, *Angew. Chem., Int. Ed.*, 2016, **55**, 12822-12826.

S11 J. Zhang, C. Du, Z. Dai, W. Chen, Y. Zheng, B. Li, Y. Zong, X. Wang, J. Zhu and Q. Yan, *ACS Nano*, 2017, **11**, 10599-10607.

S12 Z. Wei, D. Wang, M. Li, Y. Gao, C. Wang, G. Chen and F. Du, *Adv. Energy Mater.*, 2018, **8**, 1801102.

S13 J.-Y. Hwang, H.-L. Du, B.-N. Yun, M.-G. Jeong, J.-S. Kim, H. Kim, H.-G. Jung and Y.-K. Sun, *ACS Energy Lett.*, 2019, **4**, 494-501.

S14 F. Chen, D. Shi, M. Yang, H. Jiang, Y. Shao, S. Wang, B. Zhang, J. Shen, Y and Wu, Hao, *Adv. Funct. Mater.* 2020, **31**, 2007132.

S15 C. P. Wang, J. T. Yan, T. Y. Li, Z. Q. Lv, X. Hou, Y. F. Tang, H. M. Zhang, Q. Zheng and X. F. Li, *Angew. Chem., Int. Ed.*, 2021, **60**, 25013.

S16 H. Huang, R. Xu, Y. Feng, S. Zeng, Y. Jiang, H. Wang, W. Luo and Y. Yu, *Adv. Mater.*, 2020, **32**, e1904320.

S17 Ni, J.; Jiang, Y.; Wu, F.; Maier, J.; Yu, Y.; Li, L. J. Ni, Y. Jiang, F. Wu, J. Maier, Y. Yu and L. Li, *Adv. Funct. Mater.*, 2018, **28**, 1707179-1707185.

S18 H. Tao, M. Zhou, R. Wang, K. Wang, S. Cheng and K. Jiang, *Adv. Sci.*, 2018, **5**, 1801021.

S19 D. Yu, Q. Pang, Y. Gao, Y. Wei, C. Wang, G. Chen and F. Du, *Energy Storage Mater.*, 2018, **11**, 1-7.

S20 X. Zhao, H. E. Wang, X. X. Chen, J. Cao, Y. D. Zhao, Z. G. Neale, W. Cai, J. H. Sui and G. Z. Cao, *Energy Storage Mater.*, 2018, **11**, 161-169.

S21 J. L. Xia, D. Yan, L. P. Guo, X. L. Dong, W. C. Li and A. H. Lu, *Adv. Mater.*, 2020, **32**, 2000447-2000455.

S22 Z. Zhao and G. Lu, *Adv. Energy Mater.*, 2023, **13**, 2203138 .

S23 J. Wang, H. Wang, R. Zhao, Y. Wei, F. Kang and D. Zhai, *Nano Lett.*, 2022, **22**, 6359-6365.

S24 Y. H. Xiao, X. B. Zhao, X. Z. Wang, D. C. Su, S. Bai, W. Chen, S. M. Fang, L. M. Zhou, H. M. Cheng and F. Li, *Adv. Energy Mater.*, 2020, **10**, 2070113.

S25 J. Wang, X. Yue, X. Cao, Z. Liu, A. M. Patil, J. Wang, X. Hao, A. Abudula and G. Guan, *Chem. Eng. J.* 2022, **431**, 134091.

S26 L. Liang, Y. Xu, C. Wang, L. Wen, Y. Fang, Y. Mi, M. Zhou, H. Zhao and Y. Lei, *Energy Environ. Sci.*, 2015, **8**, 2954-2962.

S27 Y. Shao, M. F. El-Kady, J. Sun, Y. Li, Q. Zhang, M. Zhu, H. Wang, B. Dunn and R. B. Kaner, *Chem. Rev.*, 2018, **118**, 9233–9280.

S28 L. Yu and G. Z. Chen, *J. Power Sources* 2016, **326**, 604-612.

S29 P. Huang, H. Ying, S. Zhang, Z. Zhang and W.-Q. Han, *Adv. Energy Mater.*, 2022, **12**, 2202052.

S30 F. Niu, J. Yang, N. Wang, D. Zhang, W. Fan, J. Yang and Y. Qian, *Adv. Funct. Mater.*, 2017, **27**, 1700522.

S31 X. Li, X. Sun, X. Hu, F. Fan, S. Cai, C. Zheng and G. D. Stucky, *Nano Energy*, 2020, **77**, 105143.

S32 H. Zhang, F. Zhang, Y. Wei, Q. Miao, A. Li, Y. Zhao, Y. Yuan, N. Jin and G. Li, *ACS Appl. Mater. Interfaces*, 2021, **13**, 21217-21230.

S33 Y. Zhang, B. Wang, F. Liu, J. Cheng, X. Zhang and L. Zhang, *Nano Energy*, 2016, **27**, 627-637.

S34 Y. Jiang, Z. Jiang, M. Shi, Z.; Liu, S. Liang, J. Feng, R. Sheng, S. Zhang, T. Wei and Z. Fan, *Carbon*, 2021, **182**, 559-563.

S35 Y. Liu, X. Hu, J. Li, G. Zhong, J. Yuan, H. Zhan, Y. Tang and Z. Wen, *Nat. Commun.*, 2022, **13**, 663.

S36 D. Kim, K. Zhang, M. Cho and Y.-M. Kang, *Energy Environ. Sci.*, 2019, **12**, 1326-1333.

S37 M. Chen, P. Xiao, K. Yang, B. X. Dong, D. Xu, C. Y. Yan, X. J. Liu, J. T. Zai, C. J. Low and X. F. Qian, *Angew. Chem., Int. Ed.*, 2023, **62**, e202219177.

S38 M. Yang, X. Chang, L. Wang, X. Wang, M. Gu, H. Huang, L. Tang, Y. Zhong and H. Xia, *Adv. Mater.*, 2023, **35**, 2208705.

S39 B. Pu, Y. Liu, J. Bai, X. Chu, X. Zhou, Y. Qing, Y. Wang, M. Zhang, Q. Ma, Z. Xu, B. Zhou and W. Yang, *ACS Nano*, 2022, **16**, 18746-18756.

S40 W. Meng, Z. Dang, D. Li, L. Jiang and D. Fang, *Adv. Energy Mater.*, 2022, **12**, 2201531.